Atomic Structure of Graphene Sub-Nanometer Pores

Alex W. Robertson,[1] Gun-Do Lee,[2] Kuang He,[1] Chuncheng Gong,[1] Qu Chen,[1] Euijoon Yoon,[2] Angus I. Kirkland,[1] and Jamie H. Warner[1]*

[1]Department of Materials, University of Oxford, Parks Road, Oxford, OX1 3PH, United Kingdom

[2]Department of Materials Science and Engineering, Seoul National University, Seoul, Korea

jamie.warner@materials.ox.ac.uk;

RECEIVED DATE

ABSTRACT

The atomic structure of sub-nanometer pores in graphene, of interest due to graphene's potential as a desalination and gas filtration membrane, is demonstrated by atomic resolution aberration corrected transmission electron microscopy. High temperatures of 500 °C and over are used to prevent self-healing of the pores, permitting the successful imaging of open pore geometries consisting of between -4 to -13 atoms, all exhibiting sub-nanometer diameters. Picometer resolution bond length measurements are used to confirm reconstruction of five-membered ring projections that often decorate the pore perimeter, knowledge which is used to explore the viability of completely self-passivated sub-nanometer pore structures; bonding configurations where the pore would not require external passivation by *e.g.* hydrogen to be chemically inert.

KEYWORDS: Graphene, HRTEM, electron microscopy, defects, TEM, nanopore, filter

The introduction of nanoscale pores into graphene yields a filtration membrane that, due to the stability of its sp^2 bonding structure, is both chemically inert and exceptionally strong, all while being a single atom thick. This atomic level sieve has been experimentally demonstrated to be effective for the

desalination of water,[1] and the translocation of DNA and RNA,[2–6] and there have been theoretical studies exploring the potential use of graphene for ionic selection[7] and gas filtration.[8–12] DNA translocation is performed optimally with nanoscale pores, diameters of ~3 nm, whilst for water desalination,[13–15] gas filtration[16] and ion selection pores of sub-nanometer diameters are required. For desalination the diameter of pores in the filtration membrane are crucial as they must be small enough to reject salt ions while still permitting the passage of water molecules, with theoretical modelling studies suggesting a non-functionalized pore diameter of less than a nanometer being required.[13,17]

Synthesis of graphene-like structures with sub-nanometer pore sizes has been previously achieved through employing a bottom-up chemical synthesis technique,[18] and directly in graphene by AFM indentation,[16] however imaging these structures at the single atom level has proven problematic. Typically sub-nanometer to nanometer scale pores are created through the perforation of the graphene sheet *via* its bombardment with energetic ions[1,19,20] or electrons.[21–23] Creating pores through electron irradiation presents the advantage of both greater milling sensitivity and a high resolution *in-situ* imaging capability when performed within a TEM. Performing this process at an electron accelerating voltage of 80 kV or less permits both the sensitive control of pore creation and its safe imaging,[24,25] due to being close to the knock-on damage threshold for sp^2 bonded carbon. Achieving pores with diameters below a nanometer by this technique, however, has proven difficult. This is largely due to two factors; (i) metal adatoms catalyzing the rapid etching of the pore perimeter under continued electron irradiation, with the pore blocked by the adatom whilst at sub-nanometer diameter,[26] and (ii) the self-healing of the graphene *via* the inclusion of highly mobile surface carbon contamination into the pore.[27] These two effects are shown with aberration corrected (AC-) TEM data in Figure S1. In particular, Figure S1g and h demonstrate how sub-nanometer pores are quickly filled whilst under electron irradiation, with two consecutive images showing a sub-nanometer pore in the graphene acting as an anchor point for mobile carbon species on the surface, activated by the electron beam. Although this process can be prevented by maintaining sample cleanliness while kept under vacuum, exposure to contamination may eventually saturate pores of even nanoscale diameters, as shown in Figures S1i and j.

Here, we present the first single atom resolution images of sub-nanometer diameter pores in graphene. We achieve this through employing an *in-situ* heating holder, allowing us to heat the graphene sample to high temperatures and thus prevent the sub-nanometer pores from filling with amorphous carbon. Imaging and pore creation are performed with a JEOL 2200MCO AC-TEM at 80 kV, equipped with a monochromatic filter to reduce the beam energy spread to less than 300 meV, allowing for the single atom resolution imaging of graphene.

Results and Discussion

Heating graphene at temperatures of 500 – 800 °C allowed for the observation of sub-nanometer pores, created by irradiating the graphene at 80 kV with a high beam current density.[24] Imaging over prolonged periods of electron beam exposure was enabled by the elevated temperatures, with the high temperature preventing pore saturation by mobile surface carbons. Single atom resolution AC-TEM images of several observed sub-nanometer pore structures are presented in Figure 1, with diameters ranging from ~ 0.5 to 0.8 nm, alongside atomic models.

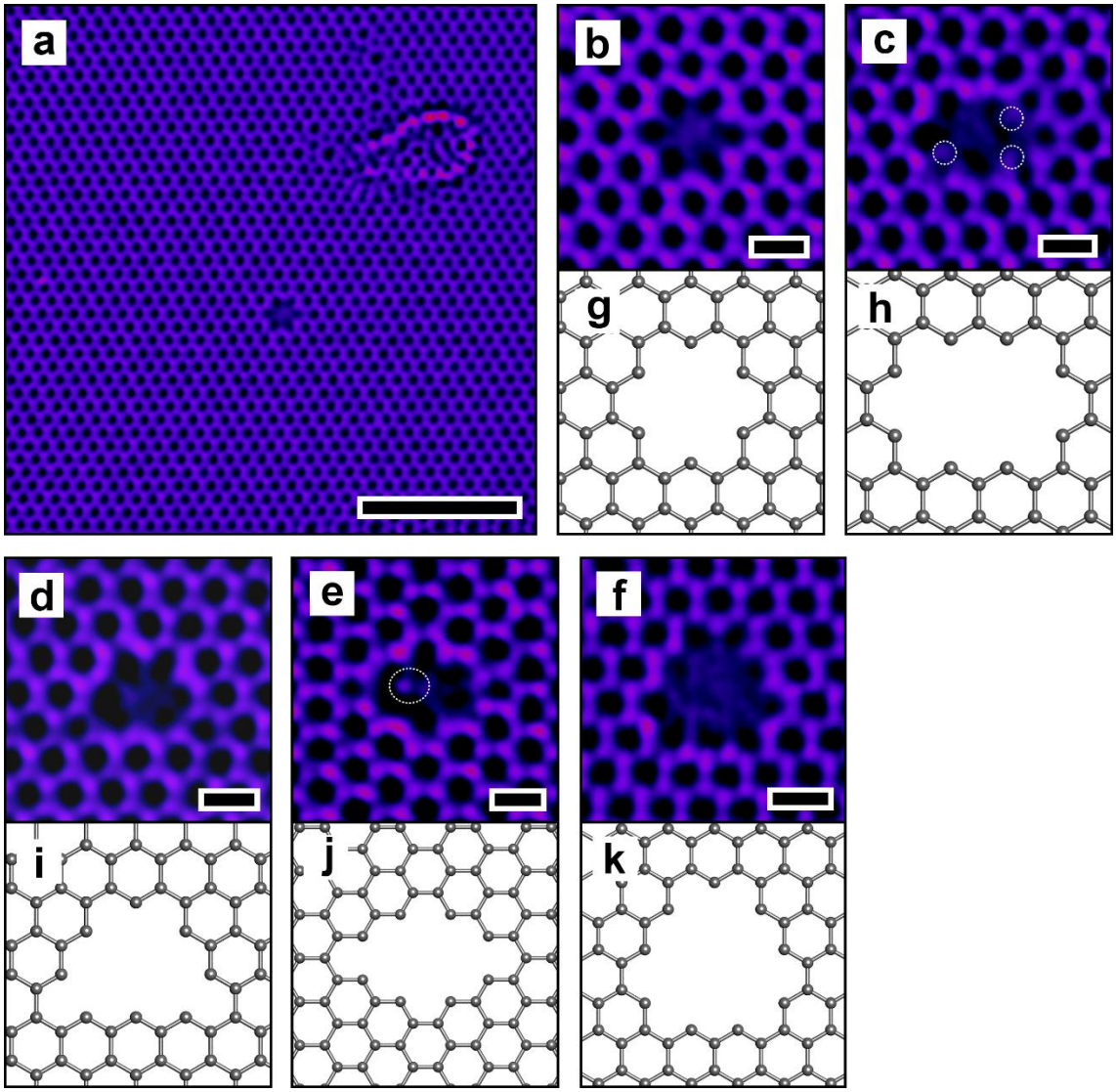

Figure 1. (a) Low and (b-f) high magnification AC-TEM images of sub-nanometer pores in graphene. (g-k) Corresponding atomic models. Dotted circles in (c) and (e) denote possible mobile atoms occupying the pore. (b) -6 atoms. (c) -10 atoms. (d) -8 atoms. (e) -8 atoms. (f) -13 atoms. Scale bars are (a) 2 nm and (b-f) 0.2 nm.

The pores were observed to grow under the electron beam *via* sequential atomic sputtering (Figure S2). The atom-by-atom process was captured, an example sequence of which is shown in Figure 2a-c. Under-coordinated atoms along the perimeter were removed preferentially, as expected due to their lower binding energy and thus higher sputtering cross section. This process lead to the formation of 5-membered rings projecting outward from the perimeter of the pore (Figure 2b and c). As with the graphene monovacancy, one would expect the two under-coordinated carbons of the five-membered ring to undergo reconstruction, removing their dangling bonds (Figure 2g). For the monovacancy, the reconstruction has

been experimentally demonstrated to reduce the inter-atomic distance to ~ 190 pm, whereas for a monovacancy with no reconstruction the distance is comparable to the equivalent bulk distance along the zigzag axis, graphene's unit cell parameter of 246 pm.[28] The inter-atomic distance between the indicated under-coordinated atoms in Figure 2b was obtained by taking a box averaged intensity profile along the boxed area in Figure 2d, which with double Gaussian fitting (Figure 2e) yielded a bond length of 205 ± 6 pm. Whilst this length is marginally larger than the monovacancy reconstructed bond it is still a significant contraction from 246 pm. Measurements of the inter-atomic distances across all single atom resolution images with of a 5-membered ring protruding along the pore perimeter were taken in the same manner, and are shown in Figure 2f, demonstrating that reconstruction does occur in almost all cases. From density functional theory (DFT) geometry optimizations on both reconstructed and non-reconstructed pores (Figure 2g and h) it was possible to model the expected atomic separations through applying the same measurement technique to multi-slice image simulations[29] (Figure 2i and j), to yield intensity profile plots (Figure 2k). These give a reconstructed bond length of 169 pm, and a non-reconstructed equivalent inter-atomic distance of 236 pm, suggesting our experimental results show weakly reconstructed five-membered rings. DFT calculations present only a small energy difference between the fully reconstructed pore (Figure 2g), with a total energy 0.51 eV less than the non-reconstructed structure (Figure 2h).

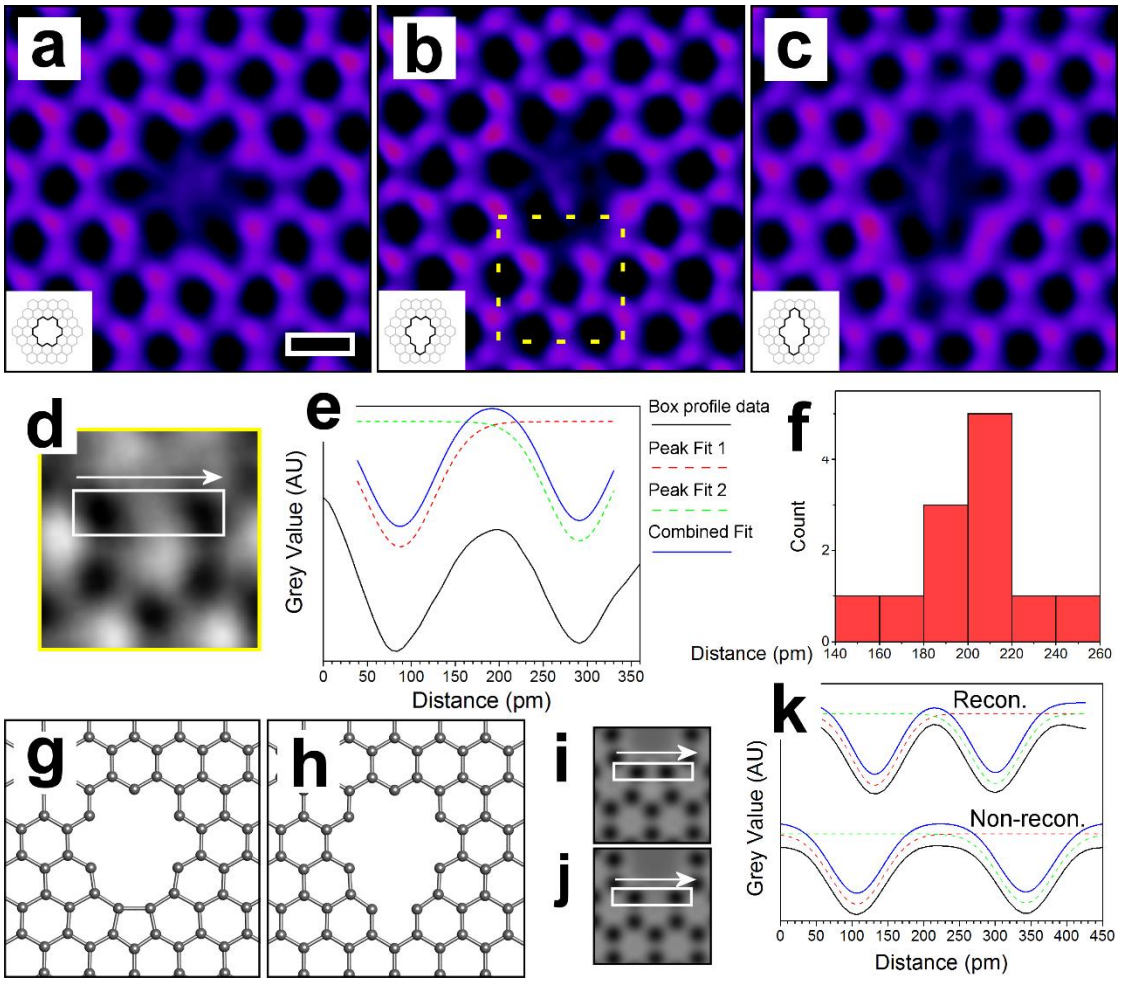

Figure 2. (a-c) AC-TEM images showing atom-by-atom growth of a sub-nanometer pore. Time stamps are (a) $t = 0$ s, (b) 65 s, and (c) 116 s. (d) Magnified view of the highlighted area in (b) (grey scale, black atom contrast). The box and arrow denote the area and direction along which the box averaged intensity profile in (e) was taken. (e) Intensity profile fitted by double Gaussians. Individual peak fits and total fit shown at different y-axis offsets, with interatomic distance of 205 ± 6 pm. (f) Distribution of measured inter-atomic distances between the under-coordinated atoms of 5-membered rings along the perimeter of imaged pores ($\bar{x}$ = 199 ± 6 pm). (g) and (h) DFT geometry optimized 7 atom pore structures for a reconstructed and non-reconstructed perimeter defect, respectively. (i) and (j) Image simulations of the perimeter defect from (g) and (h) (grey scale, black atom contrast). (k) Intensity profiles of the reconstructed and non-reconstructed perimeter defect from (i) and (j). Measured interatomic distances are 169 pm and 236 pm for the reconstructed and non-reconstructed DFT, respectively.

The pores shown in Figure 1 and Figure 2 are non-passivated, that is the under-coordinated edge carbon atoms are not saturated with hydrogen atoms or other groups,[30] as demonstrated by their tendency to

undergo reconstruction in Figure 2. Thus smaller pores of fewer removed atoms are generally unobtainable, as these will instead preferentially reconstruct into vacancy structures assembled of 4- to 8-membered rings. For instance in the case of the -4 atom pore it has been demonstrated through experiment and DFT that there is a strong preference to reconstruct into alternate tetravacancy configurations rather than remain in a more open pore shape (Figure 3a).[31] It is of interest however that the -4 atom sub-nanopore has no dangling bonds, forgoing the need for functionalization to stabilize and passivate. This is desirable, as such a pore structure can be expected to be chemically inert and thus potentially more resilient. Other possible self-passivated pore structures are shown schematically in Figure 3a, consisting of -6 and -12 atoms, respectively. AC-TEM imaging has captured several instances of the -4 atom pore (Figure 3b) but, as mentioned, this structure is not frequently observed due to alternative, more energetically favorable geometries. The postulated self-passivated -6 atom structure has been observed only once and, as shown in Figure 3c, has a substitutional dopant along the edge. The larger -12 atom pore structure was not observed at all in our high temperature data set, consisting of over 2,500 captures, and at least 300 of which contained a nano or sub-nanopore structure.

A superficial examination of the pore structures shown in Figure 3a suggests that these structures may become increasingly unstable with size as the perimeter hexagons experience larger strains, denoted with red lines in the schematics. We performed DFT structural optimization to elucidate the relative stabilities of the three self-passivated pore structures, shown in Figure 3d-f, which demonstrate that the increased strain prevents the complete reconstruction of the perimeter atoms for both the -6 and -12 atom pores. However, it is noticeable that the inter-atom separation indicated with blue arrows in Figure 3e and f increases markedly from the -6 to the -12 atom pores. Measuring the inter-atomic separation from the multi-slice TEM image simulations of the relaxed DFT structures quantifies this increase in atomic separation with pore size, as shown in Figure 3g, with the distance rising from 166 pm to 192 pm and 246 pm for the -4, -6, and -12 atom pores. The 166 pm separation found for the -4 atom pore is comparable to the 5-membered ring reconstructions in the 5-8-5 divacancy.[32] The 246 pm distance for the -12 atom pore is identical to the unit cell parameter of graphene, thus there is no interaction between the under-

coordinated perimeter atoms for the relaxed structure. The -6 atom pore occupies an intermediate position where there is some measurable degree of reconstruction between the perimeter atoms, reflected in the contracted 192 pm separation, and is comparable to measurements of the reconstructed monovacancy.[28] These results suggest that the -4 and -6 atom self-passivated pore structures should be stable and are indeed passivated through reconstructions, whereas the strain around the perimeter of the -12 atom pore would prevent the formation of reconstructions, thus will not be self-passivated. DFT of the self-passivated -6 atom pore showed an energy 2.17 eV lower than for the three-fold symmetric -6 atom pore shown in Figure 1a, again supporting the stability preference for such self-passivated structures. The low rate of observations of self-passivated -4 and -6 atom pore structures is possibly due to the action of the electron beam, which causes structures to rapidly evolve *via* Stone-Wales rotations and thus impeding their capture in a steady configuration (Figure S3).

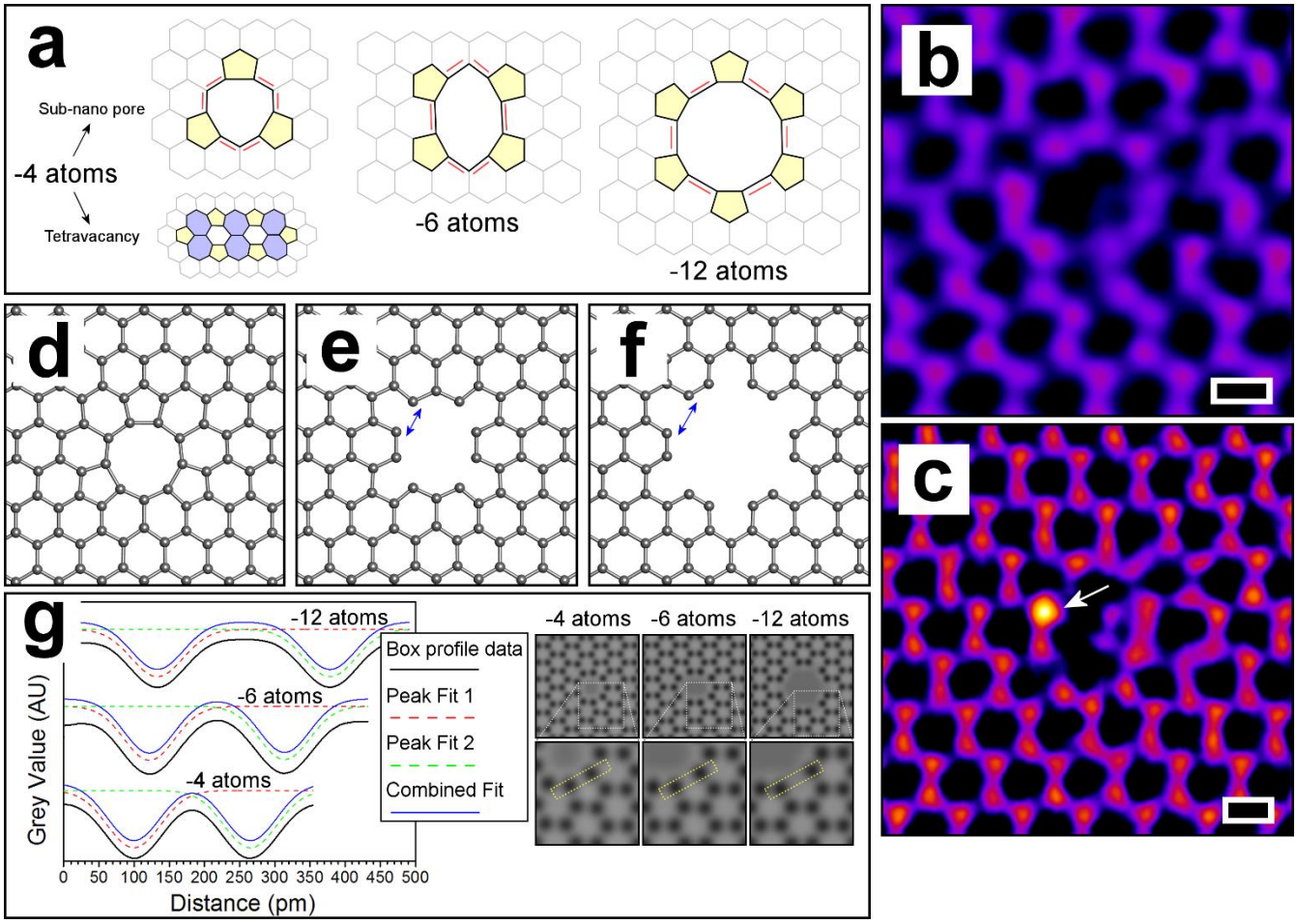

Figure 3. (a) Schematics showing the three self-passivated sub-nanometer pore structures. Red lines denote strained bonds. -4 atoms also shows the more stable tetravacancy configuration. (b) and (c) AC-TEM images of the -4 and -6 atom pore structures shown in (a). The pore in (c) has a heavy contaminant substituted for carbon at the site indicated. Scale bars are 0.2 nm. (d-f) DFT optimized geometries for the -4, -6 and -12 atom self-passivated pores, respectively. (g) Box averaged intensity line profiles with double Gaussian fittings for the inter-atomic distance indicated in the inserts for the -4, -6 and -12 atom pores. Inserts show the multi-slice TEM image simulations calculated from (d-f) (grey scale, black atom contrast) used for obtaining the intensity profile data. Individual peak fits, total fit and the three different pores are shown at different y-axis offsets. Measured inter-atomic distance are 166, 192 and 246 pm for the -4, -6 and -12 atom pore, respectively.

Recent work investigating the edges of graphene have shown that the zigzag edge (Figure 4a) preferentially configures into a reconstructed 5-7 zigzag edge at high temperature (Figure 4b).[33] Since the images of sub-nanometer pores here were captured at sufficiently high temperatures it would not be

unreasonable to anticipate that similar reconstructions may take place along the pore perimeters. However, no such 5-7 edge nanoscale pores were observed, with reconstruction of the zigzag edges only found to occur for holes with diameters over several nanometers. DFT calculation of a -6 atom pore with a 5-7 perimeter (Figure 4c) showed that the total energy was 6.01 eV greater than the non-reconstructed -6 atom pore shown in Figure 1a, explaining the lack of such structures.

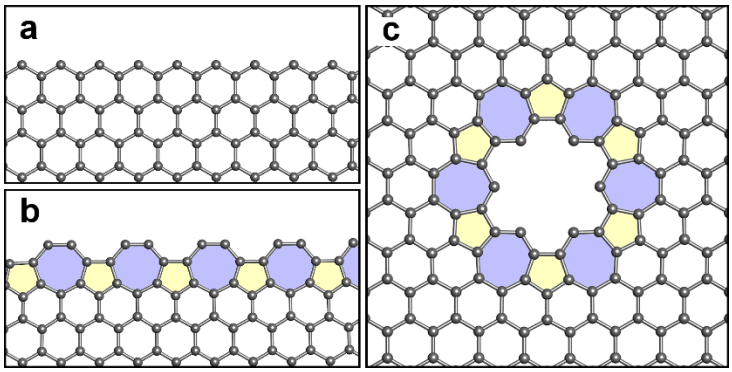

Figure 4. Atomic models of (a) zigzag edge, (b) reconstructed zigzag edge, and (c) DFT optimized reconstructed -6 atom pore.

The closest to a 5-7-5 type edge geometry that was identified was a metastable intermediate configuration that enabled 5-membered rings to migrate along the pore perimeter, with a sequential AC-TEM image series shown in Figures 5a-c. Schematic models of the images in Figures 5d-f show the -8 atom pore switching through an intermediate 5-7-5 structure (Figure 5e) *via* two Stone-Wales bond rotations (arrows). The intermediate 5-7-5 configuration along the nanopore perimeter was found to be stable, with the structure observed through several consecutive images taken over 46 seconds before switching to the configuration in Figure 5c. We suggest that frequently observed movement of five-membered rings along the pore perimeter is enabled by switching through this intermediate 5-7-5 structure, as confirmed by high temperature tight-binding molecular-dynamics (TBMD) simulations (Movie S1). These confirm the process occurs *via* two Stone-Wales bond rotations. A sequence of such pore perimeter dynamics is shown in Figures 5g-i, with the perimeter defects switching across the perimeter to particular final positions; the five-membered ring are not seen to simply move to an adjacent

site but instead a site separated by an odd number of hexagons. This is a necessary consequence of the 5-7-5 switch mechanism (see Figure S4), and supports our proposed 5-7-5 migration mechanism.

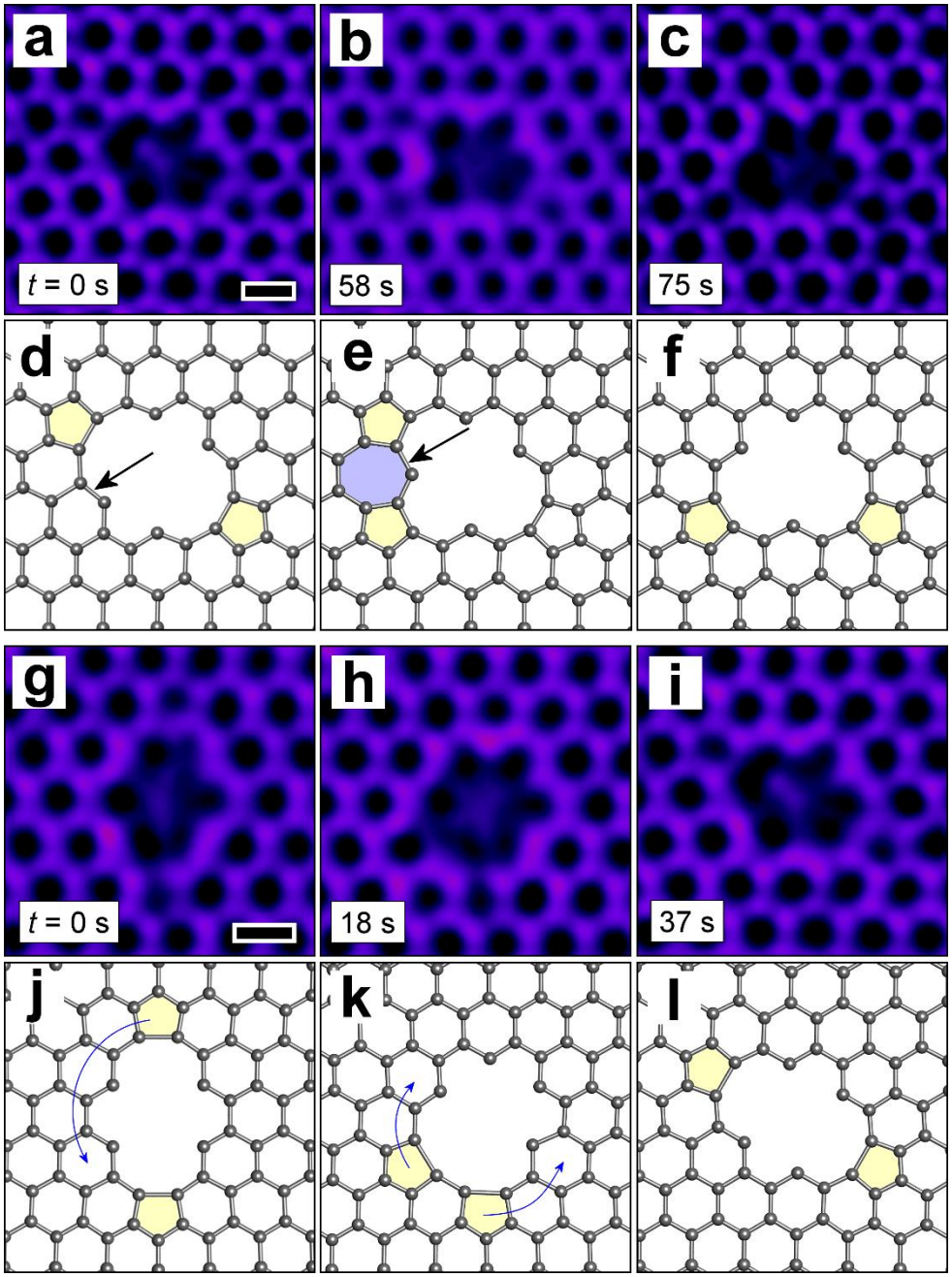

Figure 5. (a-c) Sequential AC-TEM images and (d-f) atomic models showing the translation of a 5-membered ring along the pore perimeter *via* an intermediate 5-7-5 metastable state in (e). The arrows in (d) and (e) indicate the bonds that undergo rotation. (g-i) Sequential AC-TEM images and (j-l) atomic models showing the translation of 5-membered rings along the pore perimeter. Scale bars 0.2 nm

In Figure 1c and g trace signals can be observed inside the pore, highlighted with dotted circles. We suggest that these faint signals are due to a partially mobile atom residing inside the pore. Since the atom is mobile over the course of the image exposure the registered signal is low. This is explored in more detail for the structure shown in Figure 1d in Figure 6. Figure 6a-c show the same image as in Figure 1d along with the images immediately before and after. Both Figure 6a and c are -9 atom pores, whereas Figure 6b shows an apparent -10 atom pore. Rather than an atom being ejected and another added over such a short time frame, it is more plausible that the pore in Figure 6b in fact contains an additional carbon atom that is mobile over the course of the exposure. Examination of the three sites where weak signals are seen in Figure 6b by box averaged intensity profiles (Figure 6d-h) demonstrates that the intensity of these sites (black arrows) is significantly less than that of the atoms located along the pore perimeter (red arrows). We propose that the atom is moving between metastable positions shown in Figure 6i. The importance of considering these weak signals inside the pore of mobile atoms is shown in Figure 6j-l, where a 555-777 divacancy (Figure 6j) undergoes a reconfiguration in a single frame (Figure 6k) before returning to the original configuration but translated by one lattice site (Figure 6l). The intermediate frame (Figure 6k) initially appears to that of a -6 atom pore structure if the faint inner atom signal is not taken into account.

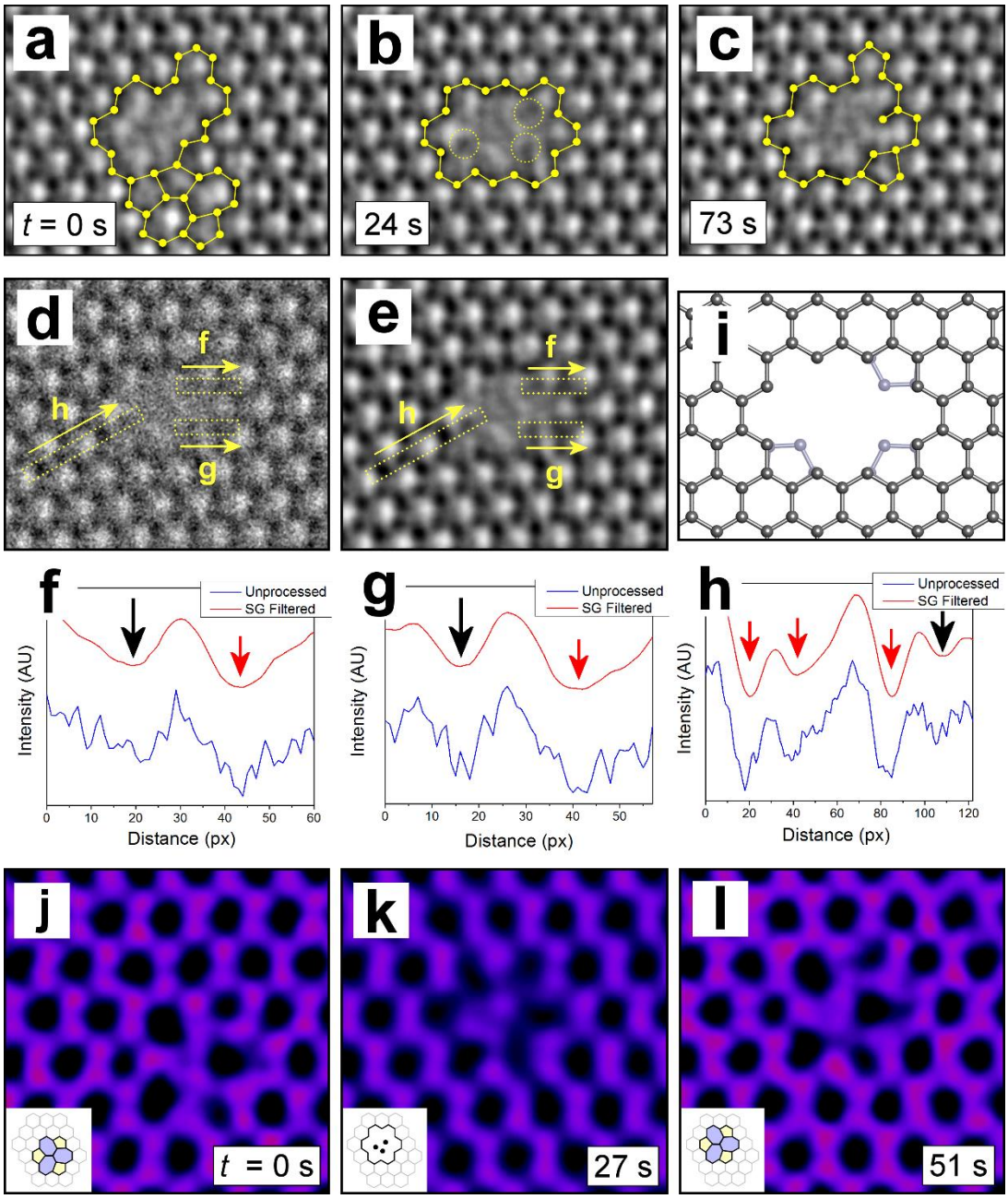

Figure 6. (a-c) Chronological AC-TEM image sequence of a sub-nanometer pore of -9, -10 and -9 atoms. Annotations denote atomic positions (images without annotations are shown in Figure S5). (d) Unfiltered and (e) Savitzky-Golay filtered image of the -10 atom pore in (b). (f-h) Box averaged intensity profiles taken along the annotated boxes in (d) and (e), with red arrows marking stable atom positions and black arrows semi-mobile inner atoms. (i) Atomic model showing the metastable sites. (j-l) AC-TEM image series showing reconfiguration of a 555-777 divacancy.

Conclusion

We have experimentally demonstrated the atomic structure of sub-nanometer pores in graphene by high temperature AC-TEM, and shown typical atomic configurations for these pores. Bond length measurements have shown that five-membered rings around the pore edge undergo weak reconstruction, with the degree of reconstruction suggesting that self-passivated -4 and -6 atom pore structures are viable. Several instances of the former and a single instance of the later were imaged, which while demonstrating their viability suggests that they are not the preferred configuration, at least when under electron beam irradiation. Although the sub-nanometer pores imaged in this report may only be stable at high temperatures and under vacuum conditions, where back-filling is reduced, our study still provides fundamental atomic level knowledge on the structure of pores that can exist in graphene at this length scale. Furthermore, our results show that edge reconstructions for these ultra-small pores is different to long straight edges, which is attributable to curvature induced strain effects. The revealing of the detailed atomic bonding arrangement of sub-nanometer pores in this work will be of assistance in understanding the reaction chemistry of graphene nano-pores.

Methods

Synthesis and Sample Preparation

Graphene was synthesized with a liquid copper catalyst CVD method as outlined in the work of Wu *et al.*.[34,35] Copper on top of tungsten was loaded into a furnace, where it was annealed at 1090 °C under 200 sccm Ar and 100 sccm H_2/Ar mix (25% H_2) gas flow for 30-60 minutes, melting just the copper. The H_2/Ar flow was lowered to 80 sccm and a CH_4/Ar mix (1% CH_4) was introduced at 10 sccm for 90 minutes. The sample was then cooled to 1060 °C for 30 minutes whilst maintaining gas flow to fill in cracks in the graphene.[35] Then the graphene was removed and quickly cooled to room temperature in a H_2 and Ar atmosphere. A PMMA support was spin coated on to the graphene/Cu/W stack before removing the metals. W was detached by attaching the sample as the anode in the electrolysis of 2 M sodium hydroxide solution with Cu as the cathode. The Cu was etch by floating the sample on 1 M ammonium

persulfate etchant, followed by extensive DI, HCl and DI water rinse stages to clean the graphene. The PMMA/graphene film was then transferred to a TEM grid. The PMMA was removed by baking in atmosphere at 350 °C overnight.

Imaging

Imaging was performed at 80 kV with Oxford's JEOL 2200 MCO aberration corrected TEM, with single atom resolution images presented here captured with the monochromator activated and using a 5 μm slit to reduce the beam energy spread to ~ 0.3 eV. A DENS Solutions heating holder was used to heat the sample to temperatures of 500 – 700 °C to permit imaging of sub-nanometer pores before being filled. Images presented in the main text have been subjected to bandpass and Gaussian or Savitzky-Golay noise reduction filters. An upper estimate of the electron flux incident on the sample is 10^5 e^- nm^{-2} s^{-1}, as found in our previous work,[24] although insertion of the monochromator slit will act to reduce this brightness. For bond measurements images have been subjected to post-correction to remove residual aberrations (Figure S6).

Modeling

The density functional theory (DFT) calculations were performed within the generalized gradient approximation (GGA) of Perdew-Burke-Ernzerhof (PBE) functional[36] using Vienna *ab initio* simulation package (VASP) code.[37] The unit cell was constructed by removing several carbon atoms from pristine graphene of 448 carbon atoms to construct odd number vacancy structures. In constructing the super cell for simulation, we contain a vacuum region of 30 Å in the *z* direction. The Brillouin zone was sampled using a (2×2×1) Γ-centered mesh. The energy cut-off used for the plane wave basis set was 400 eV. When structural relaxations were performed the structure was fully relaxed until the force on each atom was smaller than 0.02 eV/Å.

The tight-binding molecular-dynamics (TBMD) simulations were performed using a modified environment-dependent tight-binding (EDTB) carbon potential,[38] which was modified from the original EDTB carbon potential to study carbon sp^2 bond networks[39] and has been successfully applied to

investigations of various defect structures in graphene.[40–42] The details of the TBMD simulation methods have been described in previous papers.[38] The self-consistent calculations were performed by including a Hubbard-U term in the TB Hamiltonian to describe correctly charge transfers in carbon atoms of dangling bonds and to prevent the unrealistic overestimation of charge transfers. The equations of motion of the atoms were solved by the fifth order predictor-corrector algorithm with a time step of 1.0 fs. In the simulation unit cell, carbon atoms are removed from a pristine graphene lattice of 448 carbon atoms to construct defect structures. All simulations were started at a temperature of 3,000 K under the canonical control of temperature. The elevated temperature simulates the action of incident high energy electrons elastically transferring energy to carbon atoms in the graphene lattice. The temperature was gradually increased to 4,300 K under linear temperature control to accelerate the dynamics so that structural reconstruction could be observed during the simulation time. The velocity scaling method was also used to control the temperature.

Acknowledgements

JHW thanks the support from the Royal Society. AWR thanks the support from EPSRC (EP/K032518/1). G.-D.L. and E.Y. acknowledge support from the Supercomputing Center/Korea Institute of Science and Technology Information with supercomputing resources (KSC-2013-C3-058), from the BK21 plus program, and from the National Research Foundation of Korea (NRF) grant funded by the Korea government (RIAM No. 2010-0012670, MSIP No. 2013003535).

Supporting Information

Further method details, additional data and TBMD movie. This material is available free of charge *via* the Internet at http://pubs.acs.org.

References

1. Surwade, S. P.; Smirnov, S. N.; Vlassiouk, I. V.; Unocic, R. R.; Veith, G. M.; Dai, S.; Mahurin, S. M. Water Desalination Using Nanoporous Single-Layer Graphene. *Nat. Nanotech.* **2015**, *10*, 459–

464.

2. Garaj, S.; Hubbard, W.; Reina, A.; Kong, J.; Branton, D.; Golovchenko, J. A. Graphene as a Subnanometre Trans-Electrode Membrane. *Nature* **2010**, *467*, 190–193.

3. Merchant, C. A.; Healy, K.; Wanunu, M.; Ray, V.; Peterman, N.; Bartel, J.; Fischbein, M. D.; Venta, K.; Luo, Z.; Johnson, A. T. C.; *et al.* DNA Translocation through Graphene Nanopores. *Nano Lett.* **2010**, *10*, 2915–2921.

4. Schneider, G. F.; Kowalczyk, S. W.; Calado, V. E.; Pandraud, G.; Zandbergen, H. W.; Vandersypen, L. M. K.; Dekker, C. DNA Translocation through Graphene Nanopores. *Nano Lett.* **2010**, *10*, 3163–3167.

5. Garaj, S.; Liu, S.; Golovchenko, J. a; Branton, D. Molecule-Hugging Graphene Nanopores. *Proc. Natl. Acad. Sci.* **2013**, *110*, 12192–6.

6. Venkatesan, M.; Rashid, B. Nanopore Sensors for Nucleic Acid Analysis. *Nat. Nanotech.* **2011**, *6*, 615–624.

7. Sint, K.; Wang, B. Y.; Kral, P. Selective Ion Passage through Functionalized Graphene Nanopores. *J. Am. Chem. Soc.* **2009**, *131*, 9600.

8. Jiang, D. E.; Cooper, V. R.; Dai, S. Porous Graphene as the Ultimate Membrane for Gas Separation. *Nano Lett.* **2009**, *9*, 4019–4024.

9. Hauser, A. W.; Schwerdtfeger, P. Methane-Selective Nanoporous Graphene Membranes for Gas Purification. *Phys. Chem. Chem. Phys.* **2012**, *14*, 13292.

10. Schrier, J. Helium Separation Using Porous Graphene Membranes. *J. Phys. Chem. Lett.* **2010**, *1*, 2284–2287.

11. Nieszporek, K.; Drach, M. Alkane Separation Using Nanoporous Graphene Membranes. *Phys. Chem. Chem. Phys.* **2015**, *17*, 1018–1024.

12. Drahushuk, L. W.; Strano, M. S. Mechanisms of Gas Permeation through Single Layer Graphene Membranes. *Langmuir* **2012**, *28*, 16671–16678.

13. Cohen-Tanugi, D.; Grossman, J. C. Water Desalination across Nanoporous Graphene. *Nano Lett.* **2012**, *12*, 3602–3608.

14. Suk, M. E.; Aluru, N. R. Water Transport through Ultrathin Graphene. *J. Phys. Chem. Lett.* **2010**, *1*, 1590–1594.

15. Cohen-Tanugi, D.; Grossman, J. C. Nanoporous Graphene as a Reverse Osmosis Membrane: Recent Insights from Theory and Simulation. *Desalination* **2015**, *366*, 59–70.

16. Wang, L.; Drahushuk, L. W.; Cantley, L.; Koenig, S. P.; Liu, X.; Pellegrino, J.; Strano, M. S.; Scott Bunch, J. Molecular Valves for Controlling Gas Phase Transport Made from Discrete ångström-Sized Pores in Graphene. *Nat. Nanotech.* **2015**, *10*, 785–790.

17. Konatham, D.; Yu, J.; Ho, T. A.; Striolo, A. Simulation Insights for Graphene-Based Water Desalination Membranes. *Langmuir* **2013**, *29*, 11884–11897.

18. Bieri, M.; Treier, M.; Cai, J.; Aït-Mansour, K.; Ruffieux, P.; Gröning, O.; Gröning, P.; Kastler, M.; Rieger, R.; Feng, X.; *et al.* Porous Graphenes: Two-Dimensional Polymer Synthesis with Atomic Precision. *Chem. Commun.* **2009**, 6919–6921.

19. Russo, C. J.; Golovchenko, J. A. Atom-by-Atom Nucleation and Growth of Graphene Nanopores. *Proc. Natl. Acad. Sci.* **2012**, *109*, 5953–5957.

20. O'Hern, S. C.; Boutilier, M. S. H.; Idrobo, J. C.; Song, Y.; Kong, J.; Laoui, T.; Atieh, M.; Karnik, R. Selective Ionic Transport through Tunable Subnanometer Pores in Single-Layer Graphene Membranes. *Nano Lett.* **2014**, *14*, 1234–1241.

21. Lee, J.; Yang, Z.; Zhou, W.; Pennycook, S. J.; Pantelides, S. T.; Chisholm, M. F. Stabilization of Graphene Nanopore. *Proc. Natl. Acad. Sci.* **2014**, *111*, 7522–6.

22. Fischbein, M. D.; Drndic, M. Electron Beam Nanosculpting of Suspended Graphene Sheets. *Appl. Phys. Lett.* **2008**, *93*, 113107.

23. Lu, N.; Wang, J.; Floresca, H. C.; Kim, M. J. *In Situ* Studies on the Shrinkage and Expansion of Graphene Nanopores under Electron Beam Irradiation at Temperatures in the Range of 400-1200C. *Carbon N. Y.* **2012**, *50*, 2961–2965.

24. Robertson, A. W.; Allen, C. S.; Wu, Y. A.; He, K.; Olivier, J.; Neethling, J.; Kirkland, A. I.; Warner, J. H. Spatial Control of Defect Creation in Graphene at the Nanoscale. *Nat. Commun.* **2012**, *3*, 1144.

25. Meyer, J.; Eder, F.; Kurasch, S.; Skakalova, V.; Kotakoski, J.; Park, H.; Roth, S.; Chuvilin, A.; Eyhusen, S.; Benner, G.; *et al.* Accurate Measurement of Electron Beam Induced Displacement Cross Sections for Single-Layer Graphene. *Phys. Rev. Lett.* **2012**, *108*, 196102.

26. Ramasse, Q. M.; Zan, R.; Bangert, U.; Boukhvalov, D. W.; Son, Y.; Novoselov, K. S. Direct Experimental Evidence of Metal-Mediated Etching of Suspended Graphene. *ACS Nano* **2012**, *6*,

4063–71.

27. Zan, R.; Ramasse, Q. M.; Bangert, U.; Novoselov, K. S. Graphene Reknits Its Holes. *Nano Lett.* **2012**, *12*, 3936–40.

28. Robertson, A. W.; Montanari, B.; He, K.; Allen, C. S.; Wu, Y. A.; Harrison, N. M.; Kirkland, A. I.; Warner, J. H. Structural Reconstruction of the Graphene Monovacancy. *ACS Nano* **2013**, *7*, 4495–502.

29. Stadelmann, P. Image Analysis and Simulation Software in Transmission Electron Microscopy. *Microsc. Microanal.* **2003**, *9*, 60–61.

30. He, K.; Lee, G.-D.; Robertson, A. W.; Yoon, E.; Warner, J. H. Hydrogen-Free Graphene Edges. *Nat. Commun.* **2014**, *5*, 3040.

31. Robertson, A. W.; Lee, G.-D.; He, K.; Yoon, E.; Kirkland, A. I.; Warner, J. H. Stability and Dynamics of the Tetravacancy in Graphene. *Nano Lett.* **2014**, *14*, 1634–42.

32. Chen, Q.; Robertson, A. W.; He, K.; Gong, C.; Yoon, E.; Lee, G.; Warner, J. H. Atomic Level Distributed Strain within Graphene Divacancies from Bond Rotations. *ACS Nano* **2015**, *9*, 8599–8608.

33. He, K.; Robertson, A. W.; Fan, Y.; Allen, C. S.; Lin, Y.; Suenaga, K.; Kirkland, A. I.; Warner, J. H. Temperature Dependence of the Reconstruction of Zigzag Edges in Graphene. *ACS Nano* **2015**, *9*, 4786–4795.

34. Wu, Y. A.; Fan, Y.; Speller, S.; Creeth, G. L.; Sadowski, J. T.; He, K.; Robertson, A. W.; Allen, C. S.; Warner, J. H. Large Single Crystals of Graphene on Melted Copper Using Chemical Vapor Deposition. *ACS Nano* **2012**, *6*, 5010–7.

35. Fan, Y.; He, K.; Tan, H.; Speller, S.; Warner, J. H. Crack-Free Growth and Transfer of Continuous Monolayer Graphene Grown on Melted Copper. *Chem. Mater.* **2014**, *26*, 4984–4991.

36. Perdew, J. P.; Burke, K.; Ernzerhof, M. Generalized Gradient Approximation Made Simple. *Phys. Rev. Lett.* **1996**, *77*, 3865–3868.

37. Kresse, G. Efficient Iterative Schemes for Ab Initio Total-Energy Calculations Using a Plane-Wave Basis Set. *Phys. Rev. B* **1996**, *54*, 11169–11186.

38. Lee, G.-D.; Wang, C.; Yoon, E.; Hwang, N.-M.; Ho, K. Vacancy Defects and the Formation of Local Haeckelite Structures in Graphene from Tight-Binding Molecular Dynamics. *Phys. Rev. B* **2006**, *74*, 245411.

39. Tang, M.; Wang, C.; Chan, C.; Ho, K. Environment-Dependent Tight-Binding Potential Model. *Phys. Rev. B* **1996**, *53*, 979–982.

40. Lee, G.-D.; Wang, C.; Yoon, E.; Hwang, N.-M.; Kim, D.-Y.; Ho, K. Diffusion, Coalescence, and Reconstruction of Vacancy Defects in Graphene Layers. *Phys. Rev. Lett.* **2005**, *95*, 205501.

41. Lee, G.-D.; Yoon, E.; Hwang, N.-M.; Wang, C.-Z.; Ho, K.-M. Formation and Development of Dislocation in Graphene. *Appl. Phys. Lett.* **2013**, *102*, 021603.

42. Lee, G.-D.; Wang, C. Z.; Yoon, E.; Hwang, N.-M.; Ho, K. M. Reconstruction and Evaporation at Graphene Nanoribbon Edges. *Phys. Rev. B* **2010**, *81*, 195419.

TOC graphic